Virginia Polytechnic Institute and State University
Blacksburg, VA 24061

6/27/89

OPTICAL FIBER SENSORS AND SIGNAL PROCESSING FOR INTELLIGENT STRUCTURE MONITORING

FINAL REPORT

NASA GRANT NAG-1-895

JULY 1989

Prepared for: Dr. Robert Rogowski
NASA Langley Research Center
Hampton VA 23665

Prepared by: Daniel Thomas
Dave Cox
Dr. D. K. Lindner
Dr. R. O. Claus
Fiber & Electro-Optics Research Center
Bradley Dept. of Electrical Engineering
Virginia Tech
Blacksburg, VA 24061

TABLE OF CONTENTS

ABSTRACT

This report describes work carried out for NASA under grant NAG-1-895 by the Fiber & Electro-Optics Research Center at Virginia Tech. It details research conducted during the period from July 1988 to July 1989. Few mode optical fibers have been shown to produce predictable interference patterns when placed under strain. Here we describe the use of a modal domain sensor in a vibration control experiment. An optical fiber is bonded along the length of a flexible beam. Output from the modal domain sensor is used to suppress vibrations induced in the beam. A distributed effect model for the modal domain sensor is developed. This model is combined with the beam and actuator dynamics to produce a system suitable for control design. Computer simulations predict open and closed loop dynamic responses. An experimental apparatus is described and experimental results are presented.

1. INTRODUCTION

It is well known [1] that a modal domain sensor (MD sensor) can be used to sense strain in a structure. Since strain is proportional to displacement, this sensor could be used to sense vibrations in large flexible structures. Furthermore, a MD sensor could be incorporated into a control loop to actively suppress vibrations. Here we report on initial investigations into MD sensors for detecting vibrations and as a component in a control loop for active vibration suppression.

To investigate these issues, the following experiment was conducted. A flexible beam was mounted to the upright shaft of a DC servo motor. See Figure 1. As the beam is slewed through the horizontal plane, vibrations are induced. The goal of the experiment is to slew the beam from one position to another without exciting vibrations in the beam. The standard solution to this problem is to mount a sensor on the beam and accomplish the slewing maneuver by a control system which uses feedback from the vibration sensor [2]. Here we propose that the sensor be a MD sensor. The MD sensor is attached along the length of the beam, providing a distributed effect measurement of strain. A digital computer, which interfaces with the fiber signal through A/D and D/A boards, is used to execute the control law and monitor various signals. In addition, the motor has a pot and tach for position and velocity measurements of the shaft angle.

This experiment was used as a vehicle to investigate the theoretical problems of designing a control law to damp vibrations in the beam and the practical problems of implementing this design in hardware. In order to analyze the performance of the MD

sensor, a model of this sensor was developed. It is shown that the output of this sensor is proportional to the sine of the spatial integral of the strain along the fiber. For small strains, the output of the sensor is essentailly linear. For large strains, the sine nonlinearity is significant. The control law was designed assuming linear measurments, using a recently developed technique based on phase compensation [3] (See Appendix A). A detailed model of the experimental apparatus was developed and the performance of this system was analyzed. In particular simulations were performed to investigate the loss of performance due to the sensor nonlinearity.

The experimental aspects of instrumenting this sensor were also investigated. Most significantly, the use of elliptical core fiber is shown to produce a more stable intensity pattern and, hence, provides better detection than circular core fiber. The corruption of the sensor output due to the leads on and off the beam was not significant. Some drift of the intensity pattern about its operating point was seen, but this did not adversely effect the performance of the control design.

The modal domain sensing theory is developed in Section 2. The system model is presented in Section 3. Section 4 details the developement of a control law which uses the fiber signal to damp vibrations in the beam. Section 5 discusses the experimental work done with this system. Conclusions are presented in Section 6.

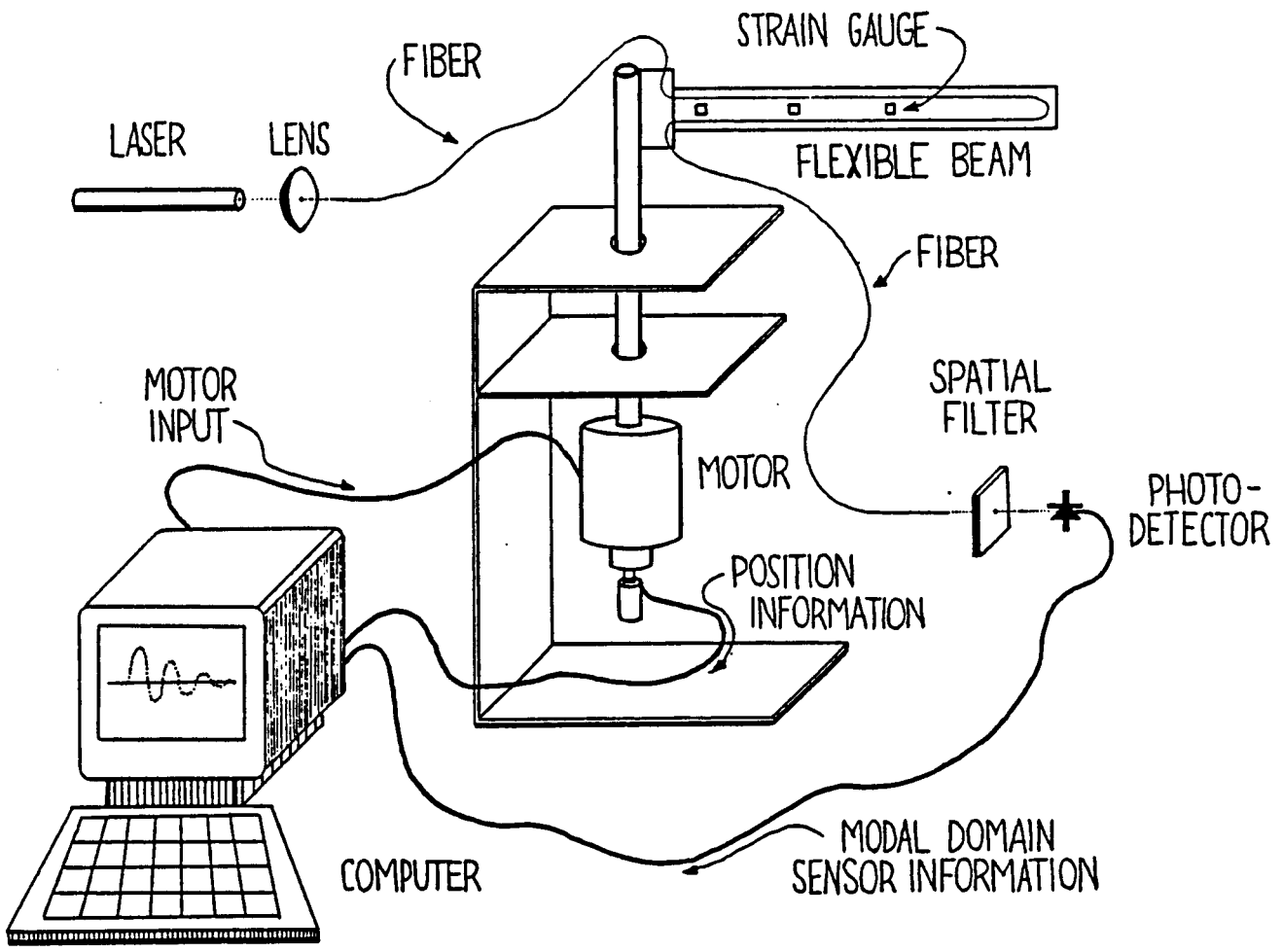

FIGURE 1. EXPERIMENTAL SETUP

2. MODAL DOMAIN SENSOR THEORY

A modal domain fiber optic sensor consists of an optical fiber, a coherent light source and detection electronics. When the fiber is illuminated with the laser a predictable intensity pattern is set up in the fiber. Disturbances to the fiber, such as applying strain, cause changes in this pattern. By monitoring these changes, information about the disturbance can be obtained. Figure 2 shows this arrangement schemetically and defines the coordinate system.

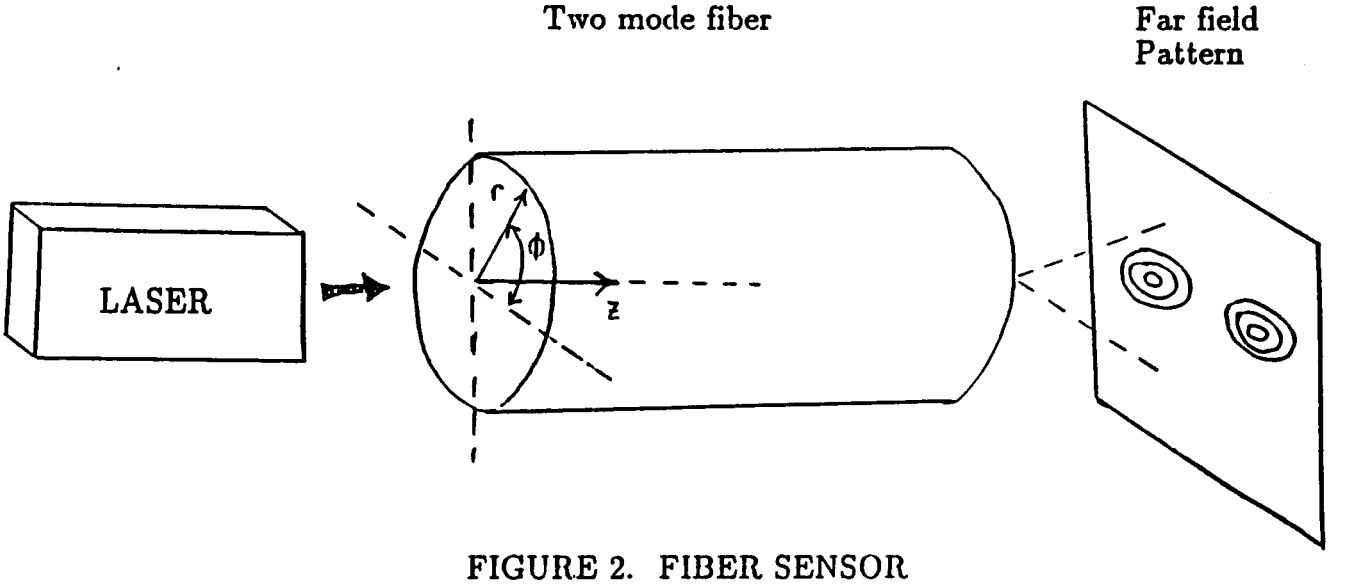

FIGURE 2. FIBER SENSOR

When monochromatic light is launched into a fiber, its power is distributed over all the possible electromagnetic modes. (An electromagnetic mode is a solution to Maxwell's equations.) The n_{th} optical mode is given by

$$\Psi_n = A_n f_n(r,\phi)\, e^{-j\beta_n z} e^{jwt} \qquad (1)$$

where

A_n= amplitude,

$f_n(r,\phi)$ = cross sectional intensity dependence,

β_n = propagation constant, and,

ω = optical frequency of the laser.

The launch conditions, fiber geometry, and the fiber materials determine whether a particular mode is excited and the value of the parameters for excited modes. These modes have different propagation constants, therefore, they travel down the fiber at different rates. This results in a far field interference pattern, which is a function of the fiber's length, at the fiber's output. When many modes are excited, no identifiable far field interference pattern is obsevered. To obtain a practical sensor arrangement, only two modes should be excited in the fiber. This is accomplished by using a 633 nm Helium-Neon laser with a fiber which is designed to have only one active mode when excited by a 820 nm laser.

When only two modes are excited in the fiber, the first mode, LP_{01}, is given by [4]

$$\Psi_0 = A_0 f_0(r) \cos(\phi)\, e^{-j\beta_0 z} e^{j\omega t}. \tag{2}$$

The second mode, LP_{11}, has even and odd degenercies which are given by

$$\Psi_1^e = A_1^e\, f_1(r) \cos(\phi)\, e^{-j\beta_1 z} e^{j\omega t}, \text{ and,} \tag{3}$$

$$\Psi_1^o = A_1^o\, f_1(r) \sin(\phi)\, e^{-j\beta_1 z} e^{j\omega t}. \tag{4}$$

If we assume that $A_1^e = 0$ then the far field intensity pattern these two modes produce is given by

$$I(r,\phi) = |\Psi_o + \Psi_1^e|^2$$

$$= |A_o|^2 f_o^2(r) + |A_1^e|^2 f_1^2(r)\cos^2(\phi) + 2|A_0||A_1^e| f_0(r) f_1(r)\cos(\phi)\cos(\Delta\beta z_o + \Delta\theta) \qquad (5)$$

where

$\Delta\beta$ - difference in propagation velocities of first and second mode,

z_o - sensor gauge length, and,

$\Delta\theta$ - initial difference in phase of the two modes.

Figure 3 shows this pattern at the fiber's endface. The intensity increases toward the center of each lobe having maximums at $\phi=0^o$ and $\phi=180^o$.

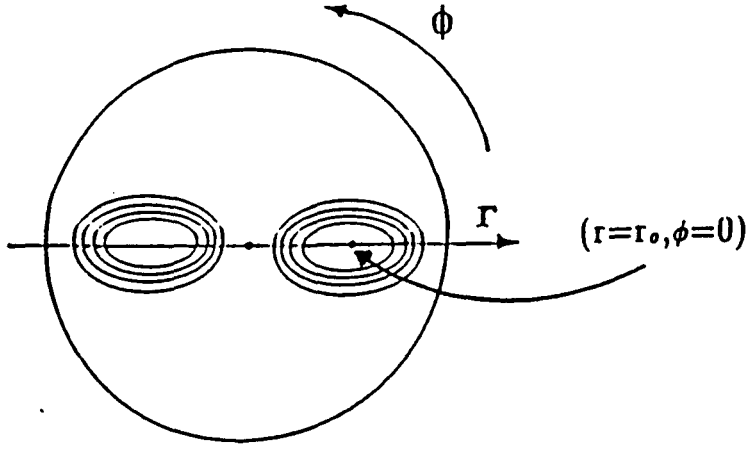

FIGURE 3. INTENSITY DISTRIBUTION

The detection scheme for this sensor involves monitoring the peak of one lobe

where $r=r_o$ and $\phi=0°$. If we assume the first mode carries approximately twice as much power as the second mode [5], the intensity at this point is given by

$$I = \frac{I_p}{2} [\, 1 + \cos(\Delta\beta z_0 + \Delta\theta) \,]. \tag{6}$$

Now if we let $\Gamma = \Delta\beta z_o + \Delta\theta$ we have an intensity variation with respect to Γ as shown in Figure 4.

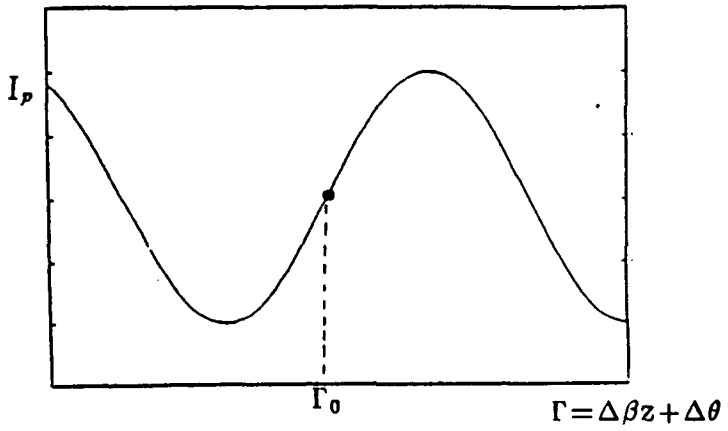

FIGURE 4. DETECTED SIGNAL VS. GAMMA

The relationship between Γ and strain includes two first order effects. One is a change in the fiber's length, and the other is a change in the index of refraction of the fiber's core. The change in Γ due to these effects is

$$\Delta\Gamma \approx \frac{\partial\Gamma}{\partial z}\Delta z \;+\; \frac{\partial\Gamma}{\partial n}\Delta n \,. \tag{7}$$

From [1] we have

$$\Delta\Gamma \approx \Delta z \,(\, \Delta\beta \;-\; \tfrac{1}{2}\, n_1{}^2\, [(1-\nu)p_{12} - \nu p_{11}] \,), \tag{8}$$

where

$\Delta z =$ elongation of the fiber,

n_1 = index of refraction of the fiber core,

ν = Poisson's ratio, and,

p_{11}, p_{12} = photoelastic constants.

The fiber's change in length can be expressed by

$$\Delta z = \int_0^{z_0} \epsilon(z,t)\, dz. \tag{9}$$

Therefore, equation (7) becomes

$$\Delta\Gamma \approx \alpha \int_0^{z_0} \epsilon(z,t)\, dz, \tag{10}$$

where α is a proportionalilty constant.

The phase term, Γ, can now be expressed as

$$\Gamma(\epsilon) \approx \Gamma_0 + \Delta\Gamma = \Gamma_0 + \alpha \int_0^{z_0} \epsilon(z,t)\, dz\ . \tag{11}$$

As seen from Figure 4, the intensity of a lobe peak varies sinusoidally with Γ. Specifically, if the fiber is prestrained to the quadrature point Γ_o=270° and the DC offset is removed, then the optical signal will vary as

$$I_f(t) = \frac{I_p}{2} \sin\Big(\alpha \int_0^{z_0} \epsilon(z,t)\, dz \Big) \approx K \int_0^{z_0} \epsilon(z,t)\, dz. \tag{12}$$

For small strains this sine term can be linearly approximated, and the fiber will produce a signal which is proportional to integral strain.

3. MODEL DERIVATION

3.1 BEAM DYNAMICS

In this section we develop the model of the instrumented beam used for the control design. We start with the flexible beam dynamics. The coordinate system that will be used is shown in Figure 5.

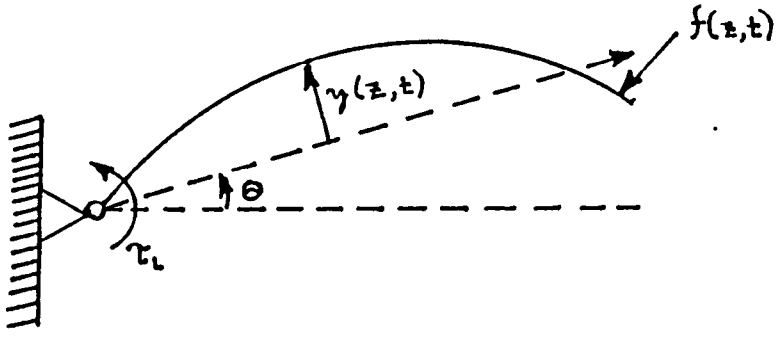

FIGURE 5. BEAM MODEL COORDINATE SYSTEM

The linear equations of motion and boundary conditions for a flexible beam with torque actuation at the hub are [2]

$$EI\frac{\partial^4 y}{\partial z^4} + \rho\frac{\partial^2 y}{\partial z^2} + \rho z\frac{\partial^2 \theta}{\partial t^2} = f(z,t)\ ,\ 0 \le z \le l\ ,\ t > 0, \tag{13}$$

$$(J_h+J_b)\frac{\partial^2 \theta}{\partial t^2} + \rho\int_0^l z\frac{\partial^2 y}{\partial t^2}dz = \tau_l(t), \tag{14}$$

$$y(0,t) = 0\ ,\ \frac{\partial y}{\partial z}(0,t) = 0, \text{ and,} \tag{15}$$

$$\frac{\partial^2 y}{\partial z^2}(l,t) = 0\ ,\ \frac{\partial^3 y}{\partial z^3}(l,t) = 0, \tag{16}$$

where

E = Young's modulus,

I = area moment of inertia about bending axis,

y(z,t) = local transverse displacement,

$\theta(t)$ = global angle of rotation,

τ_l = torque applied to the beam,

J_b = beam mass moment of inertia about the hub,

J_h = hub mass moment of inertia,

l = length of the beam, and,

ρ = beam mass per unit length.

If it assumed that the rigid body motion of the beam is fixed to an inertial frame of reference, then the global angle of rotation is constant. By setting all external forces to zero and assuming that the global angle of rotation is zero, we obtain

$$EI\frac{\partial^4 y}{\partial z^4} + \rho\frac{\partial^2 y}{\partial z^2} = 0 \ , \ 0 \leq z \leq l \ , \ t > 0. \tag{17}$$

The method of separation of variables will be used to solve this differential equation. The assumed solution to equation (17) is

$$y(z,t) = \sum_{n=1}^{N} \psi_n(z) r_n(t), \tag{18}$$

where

$\psi_n(z)$ = mode shapes, and

$r_n(t)$ = modal amplitudes.

When N=∞ we obtain the exact solution. After substituting equation (18) into equation (17) and separating the variables, we obtain

$$\frac{EI}{\psi_n(z)}\frac{\partial^4\psi_n(z)}{\partial z^4} = -\frac{\rho}{r_n(t)}\frac{\partial^2 r_n(t)}{\partial t^2} = -\kappa_n^4. \tag{19}$$

For equation (19) to be valid, both sides have to be equal for all z and t, thus they must be equal to a constant, say, κ_n^4. Expressing equation (19) just in terms of mode shapes yields

$$\frac{d^4\psi_n(z)}{dz^4} + \frac{\kappa_n^4\psi_n(z)}{EI} = 0, \tag{20}$$

$$\psi_n(0) = 0\ ,\ \frac{d\psi_n}{dz}(0)=0, \text{ and,} \tag{21}$$

$$\frac{d^2\psi_n}{dz^2}(l) = 0\ ,\ \frac{d^3\psi_n}{dz^3}(l) = 0. \tag{22}$$

Solving differential equation (20) subject to boundary conditions (21) and (22) yields

$$\psi_n(z) = C_n\ \{\cosh(\kappa_n z) - \cos(\kappa_n z) - \epsilon_n[\sinh(\kappa_n z) - \sin(\kappa_n z)]\} \tag{23}$$

where

$$\epsilon_n = \frac{\cos(\kappa_n l) + \cosh(\kappa_n l)}{\sin(\kappa_n l) + \sinh(\kappa_n l)}, \tag{24}$$

and the real numbers κ_n satisfy the characteristic equation

$$1 + \cos(\kappa_n l)\cosh(\kappa_n l) = 0\ ,\ n = 1,2,\ldots,\infty. \tag{25}$$

The time response is obtained by setting up the differential equations in terms of

$r_n(t)$. Substituting equation (18) into equations (13) and (14), we obtain

$$EI\sum_{n=1}^{N}\frac{d^4\psi_n(z)}{dz^4}r_n(t) + \rho\sum_{n=1}^{N}\psi_n(z)\frac{d^2r_n(t)}{dt^2} + \rho z\frac{d^2\theta(t)}{dt^2} = f_d(z)f(t), \text{ and,} \tag{26}$$

$$(J_b+J_h)\,\frac{d^2\theta(t)}{dt^2} + \rho\sum_{n=1}^{N}\int_0^l z\,\psi_n(z)\,\frac{d^2r_n(t)}{dt^2}dz = \tau_l(t), \tag{27}$$

where f(z,t) is expressed as a product of a spatially dependent function and a time dependent function.

Equation (27) accounts for one solution and equation (26) accounts for N solutions. Thus, to obtain the required N+1 equations for solving this system, it is convenient to multiply both sides of equation (26) by $\psi_m(z)$ and integrate over the length of the beam. This calculation yields

$$\sum_{n=1}^{N} M_{rr}^{nm}\,\frac{d^2r_n(t)}{dt^2} + \sum_{n=1}^{N} K_{rr}^{nm}r_n(t) + M_{r\theta}^{m}\frac{d^2\theta(t)}{dt^2} = B_m\,f(t)\ ,\ 0\le m\le N, \tag{28}$$

where

$$M_{rr}^{nm} = \rho\int_0^l \psi_n(z)\psi_m(z)dz = \rho l\delta_{nm}, \tag{29}$$

$$M_{r\theta}^{m} = \rho\int_0^l z\psi_m(z)dz, \tag{30}$$

$$K_{rr}^{nm} = EI\int_0^l \psi_m(z)\,\frac{d^4\psi_n(z)}{dz^4}dz = EI\,l\,\kappa_n^4\,\delta_{nm}, \tag{31}$$

$$B_m = \int_0^l \psi_m(z)\, f_d(z)\, dz, \tag{32}$$

and δ_{nm} is the Kronecker delta function. The simplifications of equations (29) and (31) come from the orthogonality property of mode shapes. Equation (31) is also simplified by the substitution of equation (19). Using this notation, equation (27) can be written as

$$(J_b + J_h)\frac{d^2\theta(t)}{dt^2} + \sum_{n=1}^{N} M_{r\theta}^n \frac{d^2 r_n(t)}{dt^2} = \tau_l(t), \tag{33}$$

where

$$M_{r\theta}^n = \rho \int_0^l z\psi_n(z)dz.$$

Equations (28) and (33) are now put into vector matrix form. Define a finite dimensional column vector r by

$$r = \begin{bmatrix} r_1 \\ r_2 \\ \cdot \\ \cdot \\ \cdot \\ r_N \end{bmatrix}. \tag{34}$$

Using this vector, the vector matrix form of the flexible beam dynamics is

$$\begin{bmatrix} J_b+J_h & M_{r\theta}^T \\ M_{r\theta} & M_{rr} \end{bmatrix} \begin{bmatrix} \ddot{\theta} \\ \ddot{r} \end{bmatrix} + \begin{bmatrix} 0 & 0 \\ 0 & K_{rr} \end{bmatrix} \begin{bmatrix} \theta \\ r \end{bmatrix} = \begin{bmatrix} 0 & 0 \\ 0 & B_m \end{bmatrix} \begin{bmatrix} \tau_l(t) \\ f(t) \end{bmatrix}. \tag{35}$$

3.2 MOTOR DYNAMICS

To incorporate the DC motor dynamics into the system, an expression is needed for the torque applied to the beam, τ_l. This expression is obtained through Newton's second law or the summation of torques about the motor shaft. Yielding

$$\tau_l(t) = \frac{K_i}{R_a} e_a(t) - J_m \frac{d^2\theta}{dt^2} - (D_v + \frac{K_i K_b}{R_a}) \frac{d\theta}{dt}, \tag{36}$$

where

J_m = rotor mass moment of inertia,

K_i = torque constant,

K_b = back emf constant,

R_a = armature resistance,

e_a = armature voltage, and

D_v = viscous frictional coefficient.

Substituting equation (36) into equation (35) yields the beam and motor dynamics as

$$\begin{bmatrix} M_{\theta\theta} & M_{r\theta}^T \\ M_{r\theta} & M_{rr} \end{bmatrix} \begin{bmatrix} \ddot{\theta} \\ \ddot{r} \end{bmatrix} + \begin{bmatrix} D_{\theta\theta} & 0 \\ 0 & 0 \end{bmatrix} \begin{bmatrix} \dot{\theta} \\ \dot{r} \end{bmatrix}$$

$$+ \begin{bmatrix} 0 & 0 \\ 0 & K_{rr} \end{bmatrix} \begin{bmatrix} \theta \\ r \end{bmatrix} = \begin{bmatrix} \frac{K_i}{R_a} \\ 0 \end{bmatrix} e_a(t), \tag{37}$$

or equivalently,

$$M \begin{bmatrix} \ddot{\theta} \\ \ddot{r} \end{bmatrix} + D \begin{bmatrix} \dot{\theta} \\ \dot{r} \end{bmatrix} + K \begin{bmatrix} \theta \\ r \end{bmatrix} = Q\, e_a(t), \tag{38}$$

where

M, D, K, and Q = coefficient matrices,

$M_{\theta\theta} = J_b + J_h + J_m$, and,

$D_{\theta\theta} = D_v + \frac{K_i K_b}{R_a}$

3.3 SENSOR MODEL

If the fiber optic sensor is attached to the beam, the strain in the beam will be transferred to the fiber sensor. Assuming that the strain induced in the fiber is equal to the beam surface strain, the output of the fiber optic sensor will measure the integral of this surface strain, equation (12). Denoting the output of the optical fiber by $I_f(t)$, we obtain

$$I_f(t) = K_o \int_0^l \epsilon(z,t)\, dz = K_o \int_0^l \frac{\partial^2 y(z,t)}{\partial z^2}\, dz\ , \tag{39}$$

or

$$I_f(t) = C_l \begin{bmatrix} \theta \\ r \end{bmatrix}, \tag{40}$$

where

$$C_l = \begin{bmatrix} 0 & C_l^1 & C_l^2 & . & . & . & C_l^n \end{bmatrix}, \tag{41}$$

with

$$C_l^n = K_o \left.\frac{\partial \psi_n(z)}{\partial z}\right|_{z=l}. \tag{42}$$

3.4 COMPOSITE MODEL

Equations (38) and (41) form a reduced order model of the instrumented beam. This model can be represented in state space form. Let

$$x = \begin{bmatrix} \theta \\ r \\ \dot{\theta} \\ \dot{r} \end{bmatrix}. \tag{43}$$

The state space model is

$$\dot{x} = Ax + Be_a \tag{44}$$
$$y = Cx,$$

where

$$A = \begin{bmatrix} 0 & I \\ -M^{-1}K & -M^{-1}D \end{bmatrix}, \tag{45}$$

$$B = \begin{bmatrix} 0 \\ M^{-1}Q \end{bmatrix}, \text{ and,} \tag{46}$$

$$C = \begin{bmatrix} 1 & 0 & \cdots & & & & & \\ 0 & \cdots & & & 0 & 1 & 0 & \cdots \\ 0 & C_l^1 & \cdots & & C_l^n & 0 & 0 & \cdots \end{bmatrix}. \tag{47}$$

The first two rows of the matrix C correspond to the potentiometer (position) and the tachometer (velocity) outputs respectively.

3.5 IDENTIFICATION

Given the model above, it was necessary to identify the parameters in the

experimental apparatus. We consider first the flexible beam. Most of the parameters in equations (13) and (14) could be measured directly. The only beam parameter which required experimental verification was the product EI. The natural frequencies of a fixed free beam are

$$\omega_n = \kappa_n \sqrt{\frac{EI}{m}}, \tag{48}$$

where

ω_n = frequency of the vibrational mode n, and,

m = mass of beam.

The beam was placed in a clamped free configuration, and disturbed such that the first few modes were excited. Output from the MD sensor was processed using a FFT algorithm, and the natural frequencies were identified. This information, along with the beam's mass, was used to back calculate the EI term from equation (48). Table 1 displays the flexible beam's parameters.

Type	Steel	
l	0.76	m
h	0.076	m
W	0.00081	m
EI	0.44	Kg^2m/s^2
Mass	0.3662	Kg
ρ	0.4818	Kg/m
J_b+J_h	0.0706	Kgm^2

TABLE 1. BEAM PARAMETERS

The DC motor being used as an actuator has the model

$$\frac{\theta}{V} = \frac{K_t}{R_a J_m s^2 + K_t K_b s}. \tag{49}$$

Only the armature resistance could be directly measured, so tests were conducted to determine the back EMF constant and armature inertia. The back EMF constant was determined by back driving the motor. A second motor was connected to the actuator shaft through a flexible coupler. The actuator was back driven at various speeds and the voltage generated at the actuator terminals was recorded. This test provided consistent results at different speeds, and produced an accurate value for the back EMF constant. Since a DC motor can be operated as either a generator or a motor, the torque contant and the back EMF constant relate the same fundamental parameters. The constants are equal in value, but have different units.

Since the armature inertia was the only parameter left to be determined, it was computed from the motor's frequency response. The technique used to develope the motor's frequency response involved driving the motor with a wide band noise source. The source data was digitally generated and a FFT of the data showed that it possessed a relatively even distribution of power in the frequency range of interest. This data was output through an A/D board to the motor. With this noise driving the motor, data was collected from the tachometer and digitally stored. The input and output data was then processed via a FFT algorithm. A plot of this frequency response is shown in Figure 6. The transfer function was fit to the noise test curve and a value was determined for the rotor inertia.

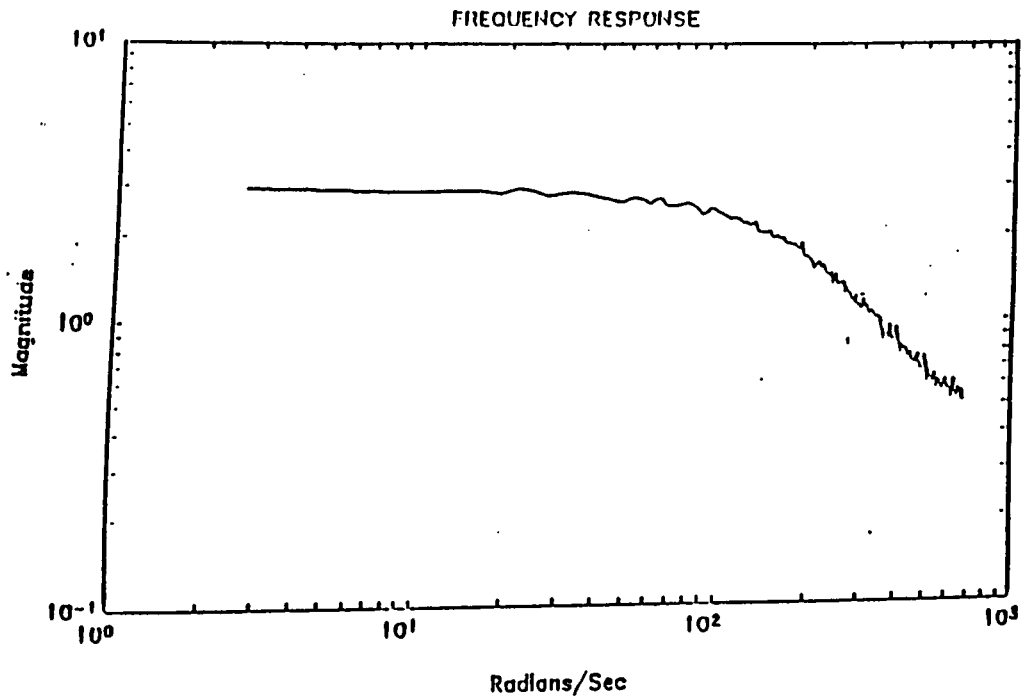

FIGURE 6. EXPERIMENTAL FREQUENCY RESPONSE

With all of these parameters experimentally determined, the linear motor model was complete. Table 2 displays the motor parameters.

R_a	5.2	Ω
K_b	0.288	V s/rad
K_t	0.288	N m/A
J_m	1.32×10^{-4}	Kg m^2

TABLE 2. MOTOR PARAMETERS

In order to include nonlinear effects in the system simulation, another motor test was performed. The motor was driven with a range of DC voltages and the velocity was

recorded corresponding to each voltage. This data is shown in Figure 7. The motor's deadband was set at 2.0 volts since no significant motion occured at voltages below this level. The saturation was an abrupt cutoff since it was due to the amplifier and not the motor. The amplifier had negligible dynamics, therefore its gain and saturation characteristics are lumped together with the motor model.

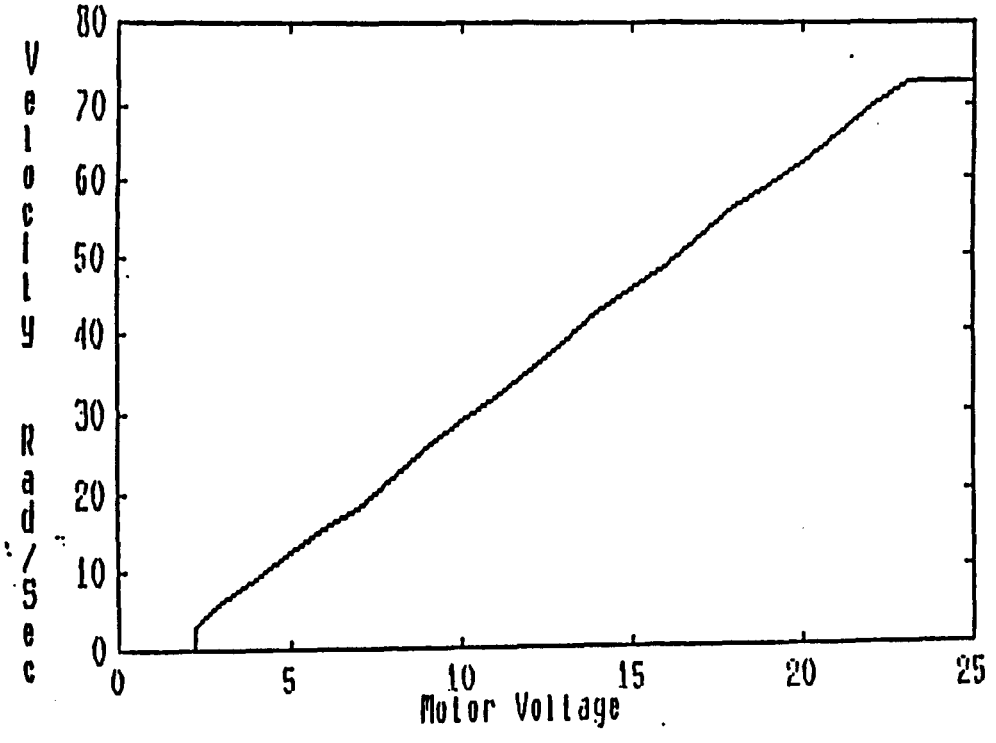

FIGURE 7. NONLINEAR MOTOR RESPONSE

4. CONTROL SYSTEM DESIGN

4.1 CONTROL LAW

Once an accurate model of the system had been developed a control law was designed to tailor the systems dynamic performance. The control law has three nested loops. The first two loops employed gain feedback on position and velocity of the shaft. These gains were obtained by considering the tradoff between rise time and overshooot of the motor shaft.

With these loops closed, a dynamic compensator was designed to suppress vibrations in the beam using the fiber signal as an input. This compensator was designed using phase compensation techniques [3], see Appendix A. For design purposes only three vibrational modes were included in the system model. Figure 8 is a root locus of the system when position and velocity loops have been closed. This system will be refered to as the uncompensated system since no vibrational control has been attempted. The lines show movement of the poles as gain feedback is applied to the fiber signal.

Since both positive and negitive gain feedback drive the system unstable a dynamic compensator must be placed in the feedback loop. The damping in a system is a function of the real part of the poles. Poles which lie far in the left half plane describe vibrations which decay quickly. Therefore, we desire each pole to depart at an angle of 180 degrees, traveling into the left haft plane with increasing gain. In this system, the change in a poles departure angle with the addition of a compensator can be approximated by the phase of the compensator at the frequency of the pole. To achieve

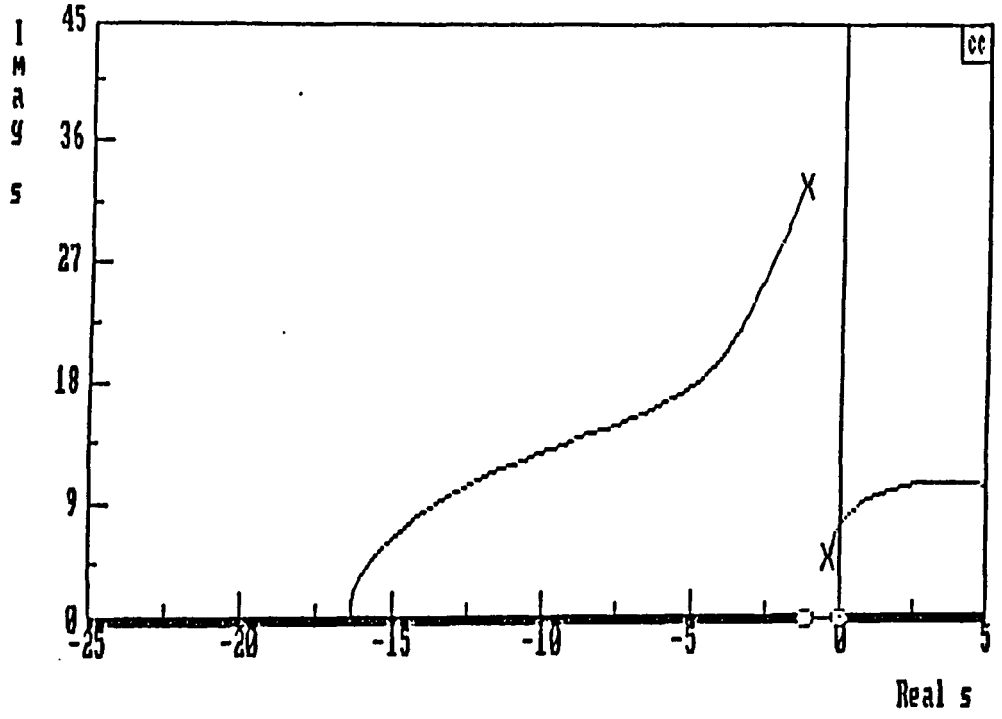

FIGURE 8. UNCOMPENSATED ROOT LOCUS

a 180 degree departure angle in the dominate poles we need to add about 60 degrees of phase at 5 radians per second, and add about 45 degrees of negitive phase at 31 radians per second. A low order compensator which approximated these phase characteristicsis is given by

$$G(s) = \frac{s+2}{(s+7)(s+30)}. \tag{50}$$

Figure 9 is a bode plot of this compensator. Less than 60 degrees of phase is added to the first pole, but this leads to an increase in frequency as well as damping when gain is applied. Since this pole dominates the system's time response an increase in frequency helps to improve the settling time.

The compensated root locus is shown in Figure 10. The boxes show closed loop pole locations for a particular gain setting. The first poles had an increase of 16% in

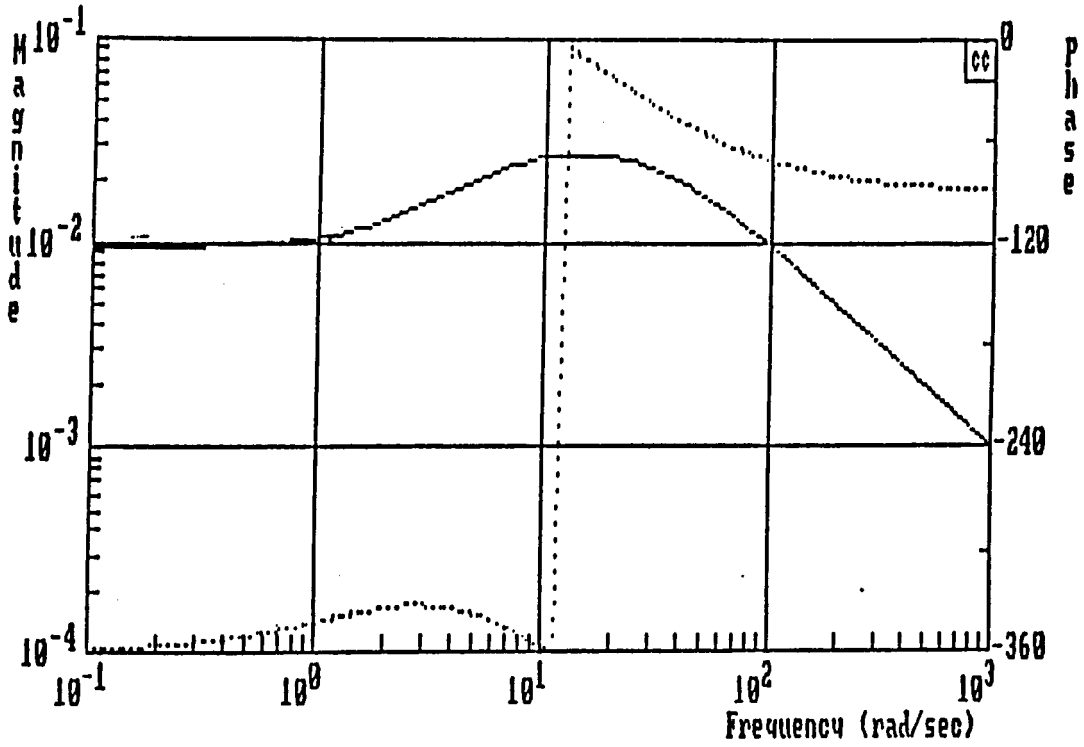

FIGURE 9. COMPENSATOR FREQUENCY RESPONSE

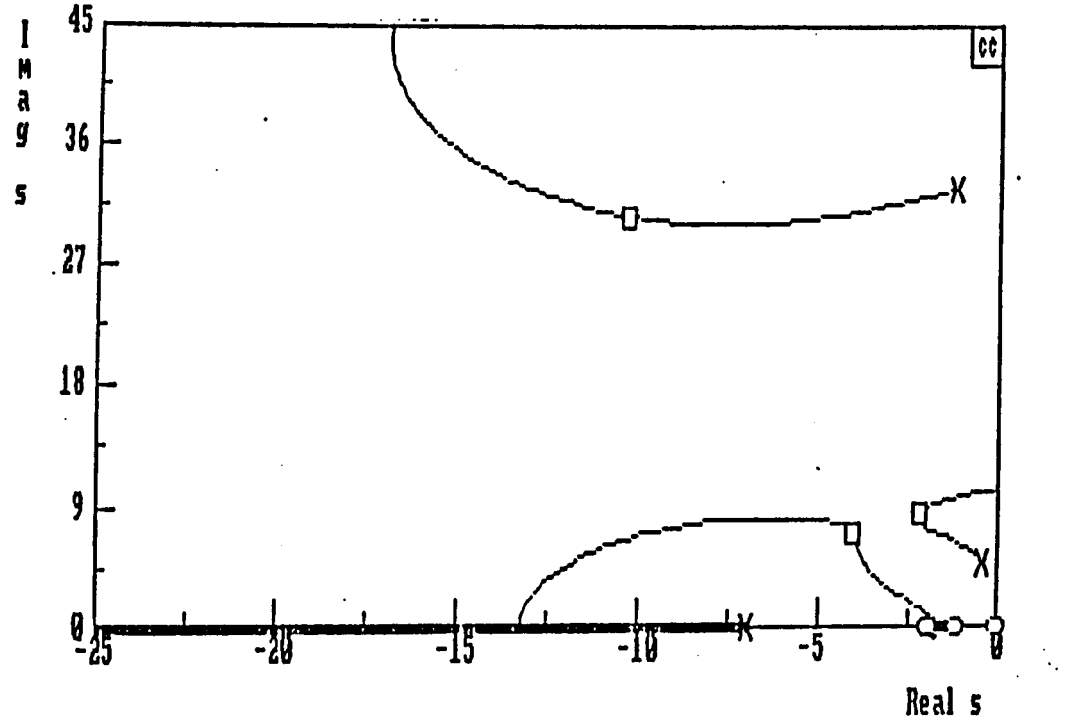

FIGURE 10. COMPENSATED ROOT LOCUS

damping, and the second had an increase of 28% in damping over the uncompensated system. To check the robustness of this control law the compensator was applied to a sixth order model. The low order poles exhibted the same increase in damping as in the three mode model. The higher poles were essentially uneffected. A loss of .5% damping was seen in the third set of poles and a loss of .2% damping in the fifth set of poles. The fourth and sixth poles experienced a slight increase in damping.

4.2 SIMULATION RESULTS

A simulation program was developed which uses the system model to predict dynamic response to various inputs. A set of difference equations is used to implement the control law, and these equations are sampled at a rate which is feasible in the experimental setup. The effect of the cosine term in the fiber's signal is included in the simulation, as well as saturation nonlinearties from the motor. The motor model, however, was considered linear at low voltages.

Figure 11 shows the fiber signal for open and closed loop step responses. The closed loop response, shown in dotted lines, settles out much faster than the open loop response. This indicates a quicker suppression of vibrations during the same maneuver. The tip position during this same slew is shown in Figure 12. Again the closed loop response has a much faster settling time, and a slightly faster rise time. These results indicate good performance from the fiber sensor, however, the size of this slew was kept very small in order to keep the fiber within its linear range. In order to see the effect of this nonlinear sensor a large angle slew maneuver was simulated.

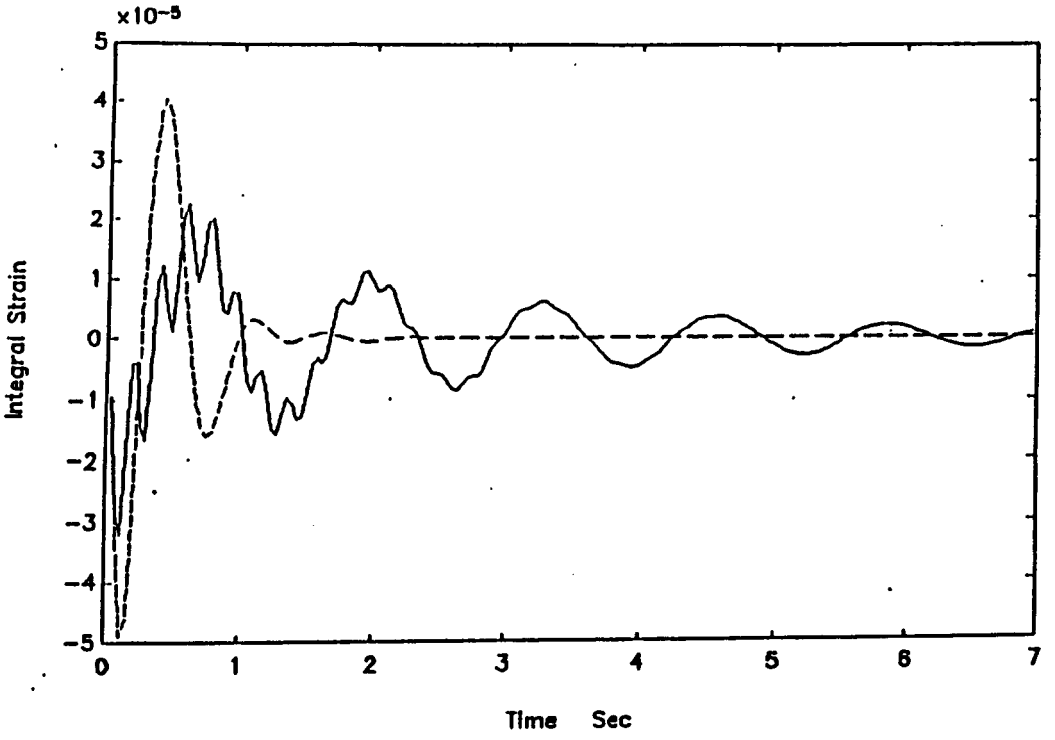

FIGURE 11. OPEN AND CLOSED LOOP FIBER SIGNAL

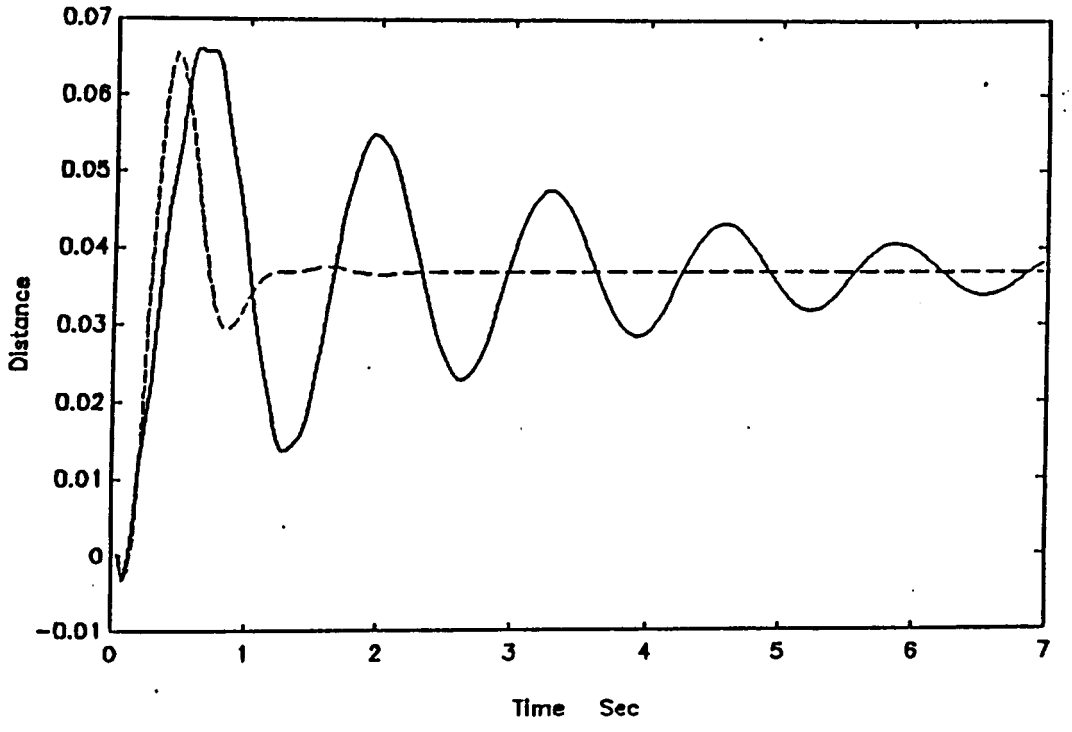

FIGURE 12. OPEN AND CLOSED LOOP TIP POSITION

Figure 13 shows the fiber signal for the open and closed loop cases when the slew angle is large. During the first few seconds, the fiber signal oscillates and does not accurately reflect the beam's vibrations. Due to natural damping in the system the beam's vibrations eventually return to the linear range of the fiber. When this ocurrs the control scheme becomes effective and damps the vibrations as before. This effect is seen more clearly from the tip position plot shown in Figure 14. During the first few seconds of vibration, the open and closed loop responses match almost exactly. Then, once the vibrations enter the fiber's linear range, the tip position settles quickly to the rigid body position.

These simulations demonstrate the ability to use the MD sensor in a control system. The main limitation of the fiber, in this application, is the nonlinear response

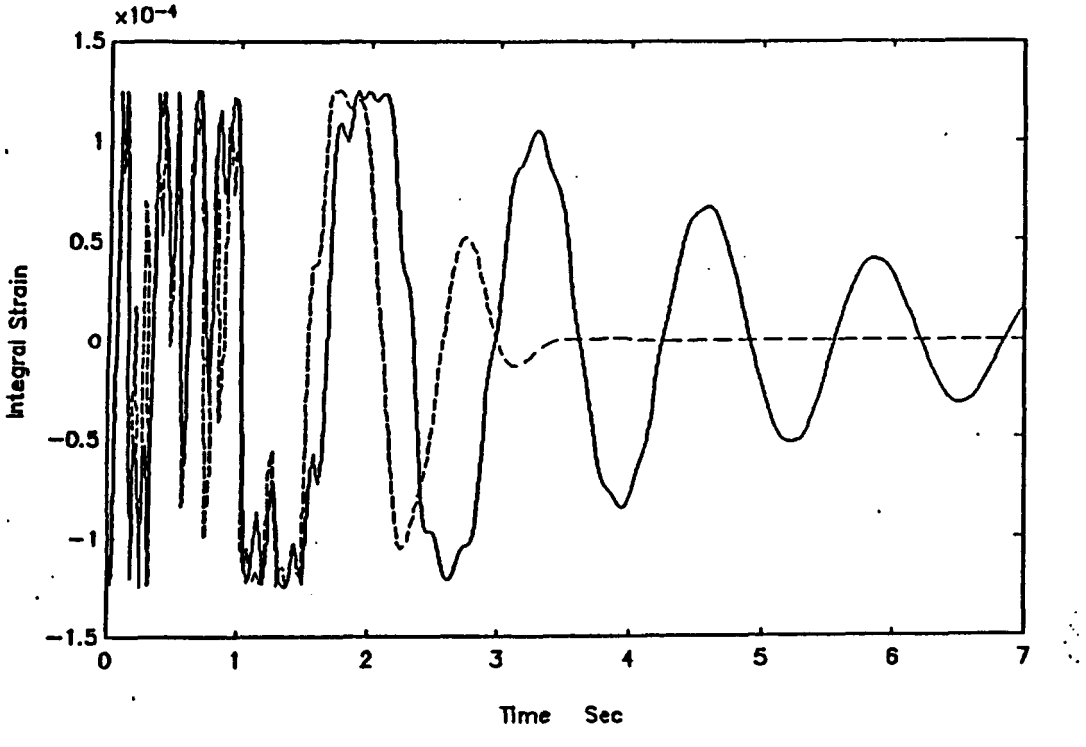

FIGURE 13. OPEN AND CLOSED LOOP FIBER SIGNAL

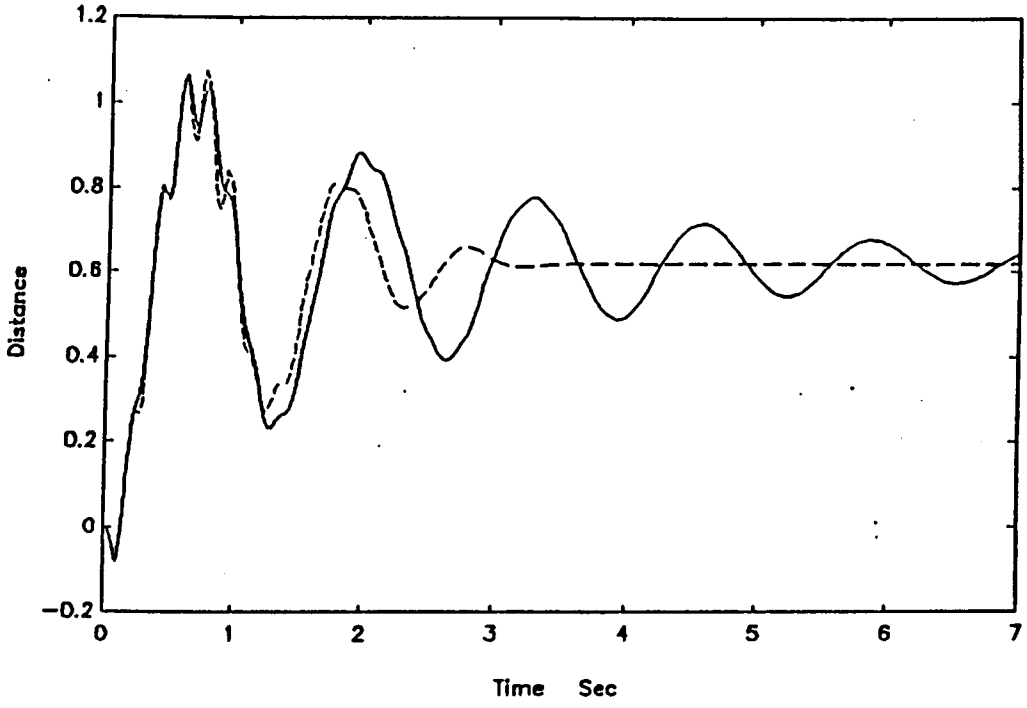

FIGURE 14. OPEN AND CLOSED LOOP TIP POSITION

under large strain. The saturated signal, however, did not drive the system unstable. In fact the open and closed loop performance were equivelent for large vibrations. This behavior is under investigation.

5. EXPERIMENTAL RESULTS

5.1 OPTICS

The experimental apparatus described in Section 1 was used to test the theoretical results above. In this section, we describe these results. The first problem encountered in using the fiber optic strain sensor was one of modal stability. The dual mode fiber actually supports three linearly polarized modes, these are the LP_{01} and the even and odd LP_{11} degenerate modes. Degenerate modes have the same propagation velocities, however, the modes have different spatial orientations with respect to the fiber endface. Under the presence of strain, power is coupled into these degenerate modes. Each LP_{11} mode has a two lobe pattern which shifts its orientation when coupling occurs. This causes a distortion of the far field pattern, and ultimately results in incorrect measurements of the induced strain.

Research carried out at Stanford University [6,7] suggested that an elliptical core fiber could prevent coupling into the LP_{11} degenerate modes. This decoupling occurs because the asymetrical geometry of the elliptical core fiber causes the even and odd LP_{11} modes to have different propagation velocities. Because of this change in propagation velocities, the even LP_{11} mode is not allowed to propagate if the fiber parameters are carefully chosen. This fiber exhibited a stable two lobe pattern, and proved to be reliable under both static and dynamic tests [8]. Experimental data suggests that the elliptical core fiber is about three times as sensitive as circular core fiber.

The second potential problem encountered was one of instrumenting the beam with

the optical fiber. The fiber senses strain along its entire length, therefore, the leads which go from the laser to the beam and from the beam to the photodetector will pick up extraneous strain. Since the beam is to be slewed, these leads will move and introduce noise into the sensor signal. To reduce this noise, a nonsensing lead was used to go from the beam to the photodetector. The lead was a large core optical fiber placed in the far field pattern of the elliptical core fiber. The large core fiber was aligned to receive a portion of one of the two far field lobes. Thus, this fiber serves as both a spatial filter of the output pattern, and as a waveguide to carry light to the photodetector. Since the large core fiber carries amplitude information only, phase shifts due to extraneous strain will not effect its performance. It was found that with one nonsensing lead, the noise due to extraneous strain was negligble. Therefore, a nonsensing lead from the laser to the beam was not instrumented.

5.2 TEST DATA

The control law designed in Section 4 was implemented on the experimental setup. Figure 15 shows the open and closed loop fiber signals for a typical step response. In the first second, the vibrations were large and the fiber signal was nonlinear. Natural damping in the system allowed the fiber to return to its linear range and the control law became effective. However, the torques required to supress these small vibrations were small and corresponded to the motor's nonlinear region. After about 5 seconds the open and closed loop responses match, indicating that the motor voltages are below the deadband and the actuator has no effect.

A second motor was obtained which had better deadband characteristics. In addition the motor was equipted with a 35:1 gear box. The gear box allowed the motor

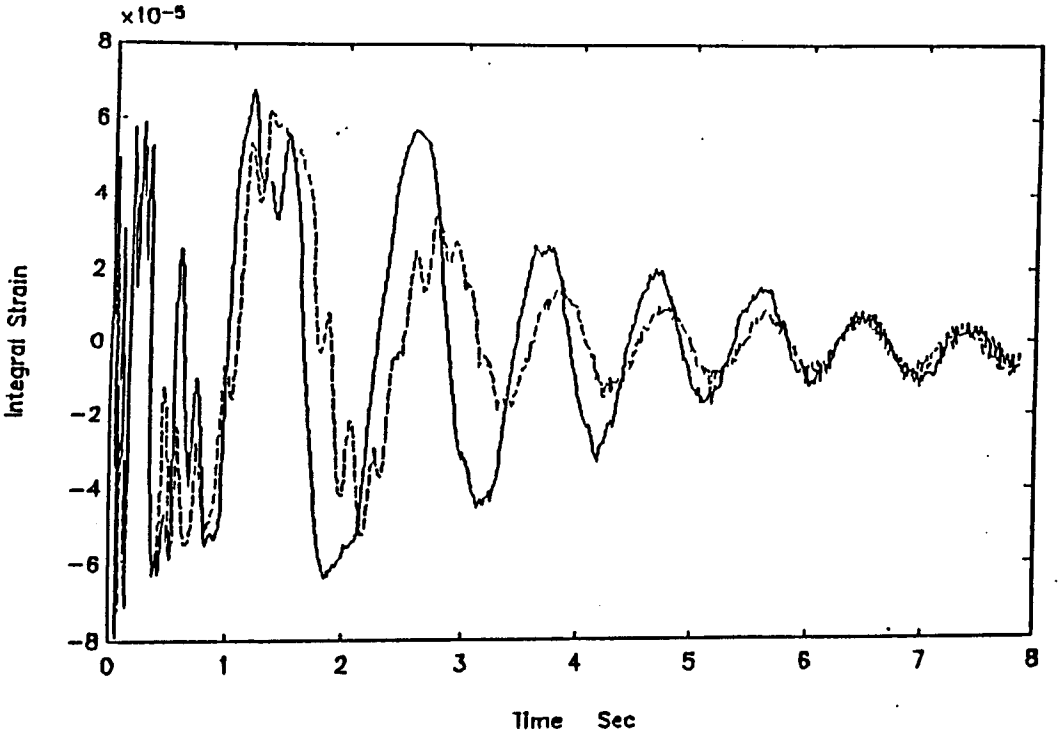

FIGURE 15. OPEN AND CLOSED LOOP FIBER SIGNAL

to operate at higher speeds and isolated it from the effects of the beams vibrations. This motor was incorporated into the system model and a new control law was designed in the same manner as before. The open and closed loop responses are compared in Figure 16. The results of these experiments were slightly better than with the orginal motor, however, backlash in the gearbox prevented accurate control of the beam. The vibrations are damped in the first two seconds of the step response. After this point small oscillations remained which could not be controlled.

These results illustrate the limitations in control system design imposed by the nonlinearities of the hardware; specfically, the nonlinearties of the sensor and actuator. Our laboratory experience indicates that within its linear range the MD sensor will produce accurate clean signals approiate for use with feedback control. This knowledge, and the simulation results, encourages the use of MD sensors for vibrational control.

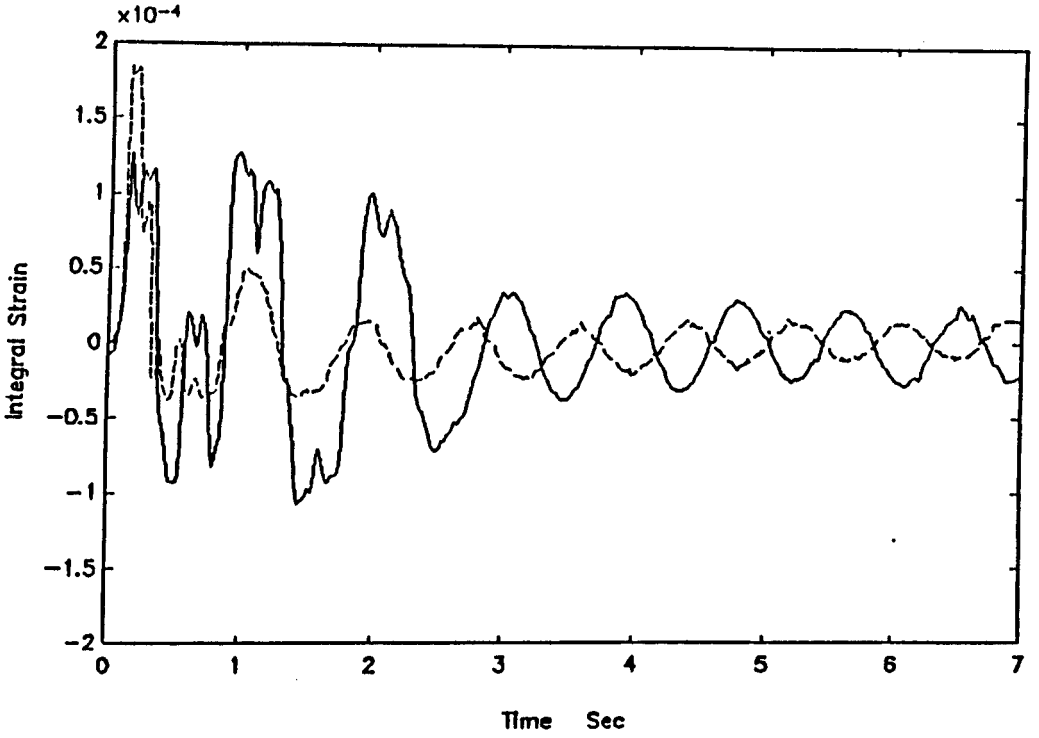

FIGURE 16. OPEN AND CLOSED LOOP FIBER SIGNAL

6. CONCLUSION

This research has demonstrated, theoritically and experimentally, the feasibility of using MD sensor for dynamic sensing of vibrations in flexible structures and as a component in an active control system to damp those vibrations. This work included the development of a model for the MD sensor and the experimental implementation of the sensor.

Because of the hardware limitations, the experimental results were somewhat limited. Current research effort is directed at redesigning the vibrational control experiment and verifying the MD sensor models. Detection schemes, which monitor the full far field pattern and employ optical processing, are being investigated to improve the stability of the sensor's signal. Coupling of strain from the structure to the fiber needs to be researched for both bonded and embedded fibers. Finally, tailoring the fiber such that it has sensing and nonsensing sections will allow detection of vibrations in an isolated part of a structure.

REFERENCES

1. C. Butter and G. Hocker, "Fiber Optics Strain Gauge", Applied Optics, vol. 17, 1978, pp. 2867-9.

2. E. Barbieri, and U Ozguner, "Unconstrained and Constrained Mode Expansions for a Flexible Slewing Link", ASME Transactions, Journal of Dynamic Systems, Measurement and Control, December 1988, pp. 416-421.

3. T. Celano and D. Lindner, "Design of Low Order Compensators for Vibration Suppression in Flexible Structures", submitted to Journal of Guidance, Control, and Dynamics, June, 1989.

4. A. Safaai-Jazi and R. O. Claus, "Synthesis of Interference Patterns In Few-Mode Optical Fibers", SPIE Proceedings on Fiber Optic Smart Structures and Skins, (Boston MA), 1988, pp. 180-185.

5. B. Duncan, Model Interference Techniques for Strain Detection in Few-Mode Optical Fibers, Masters Thesis, Bradley Department of Electrical Engineering, Virgina Tech, 1988.

6. B. Y. Kim, et. al. , "Use of Highly Elliptical Core Fibers for Two-Mode Fiber Devices", Optics Letters, vol. 12, no. 9, September 1987.

7. J. N. Blake, S. Y. Huang, B. Y. Kim, and H. J. Shaw, "Strain Effects on Highly Elliptical Core Two-Mode Fibers", Optics Letters, vol. 12, no. 9, September 1987.

8. K. D. Bennett, J. C. McKeeman, and R. G. May, "Full Field Analysis of Modal Domain Sensor Signals for Structural Control", Proceedings from SPIE International Symposium and Exhibition on Fiber Optics, Optoelectronics and Laser Applications, (Boston MA), September 1988.

APPENDIX A

Design of Low Order Compensators for Vibration Suppression in Flexible Structures*

by

Thomas P. Celano and Douglas K. Lindner

Bradley Department of Electrical Engineering
Virginia Polytechnic and State University
Blacksburg, VA 24061

ABSTRACT: It was recently proposed that proper second order compensators could be used to stabilize and add damping to the vibrational modes of a flexible structure. Here we develop a procedure for designing these compensators based on classical techniques. This procedure generalizes the previous design procedure.

*This work was supported in part under NASA Grants NAG-1-895 and NAG-1-840

Introduction

There has been considerable interest recently in active feedback control for vibration suppression in flexible structures. This control problem is characterized by the presence of poles near the imaginary axis. The first step in the control design is to use a feedback loop to add damping to these poles. Recently, Wie and Byun[1] proposed the use of second order compensators to achieve this damping. Here we elaborate on that design technique.

In this note we present a procedure for choosing a compensator and a justification for this procedure. Two examples illustrate the procedure. As a result of this analysis, we show that the compensator pole–zero structure is not restricted to those presented by Wie and Byun[1]. The results here are based on an apparently little known compensation technique for power systems[2].

Discussion

In this note we consider the plants described by the single input single output transfer function

$$P(s) = \frac{Y(s)}{U(s)}. \tag{1}$$

We assume that P(s) is stable, however, it has poles, $p_i = \alpha_i + j\omega_i$, $i = 1,2, \cdots m$, with small damping. That is, the poles p_i are close to the $j\omega$–axis. We consider the problem of designing a negative unity feedback control system with cascade compensator C(s) (See Fig. 1) to add damping to the poles, p_i, of P(s). We also assume that the physical constraints of the problem imply that the control system will have relatively low loop gain. These assumptions are typical of vibration suppression problems in large space structures. The flexibility of the structure introduces poles close to the imaginary axis. Additional poles and zeros away from the imaginary axis may be introduced by the sensor and actuator dynamics. Finally, most current actuators are relatively low authority.

In the design approach described below, the compensator C(s) is chosen using root locus arguments to adjust the departure angle of each vibrational mode pole of P(s) such that this departure angle is approximatley 180°. For low gain, this departure angle maximizes the amount of damping introduced into that mode.

The departure angle of a pole is determined by selecting a test point near the pole in question and

determining the total angular contribution of the poles and zeros of P(s) (See Fig. 2). If the test point is on the loci, it satisfies the formula

$$\sum \text{angles from the zeros} - \sum \text{angles from the poles} = 180. \tag{2}$$

Let ϕ_i be the departure angle of the pole p_i when C(s) = constant. If C(s) is allowed to be dynamic, then (2) reduces to

$$\phi_i + \sum \text{angles from zeros of C(s) to } p_i - \sum \text{angles from poles of C(s) to } p_i = \phi_{di} \tag{3}$$

where ϕ_{di} is the departure angle of p_i after the introduction of the dynamic compensator C(s). Now if $j\omega_i$ is the imaginary part of the pole p_i, then, using standard complex function theory, we note that

$$\arg(C(j\omega_i)) = \sum \text{angles from zeros of C(s) to } j\omega_i - \sum \text{angles from poles of C(s) to } j\omega_i. \tag{4}$$

Thus, the phase of the compensator C(s) at the resonant frequency of the pole p_i can be used to approximately determine the departure angle of the pole when α_i is small.

The observation above leads to the following design procedure.

1. Determine the departure angles ϕ_i.
2. Determine the desired departure angles ϕ_{di}, usually 180°.
3. Determine the desired compensator phase $C(j\omega_i)$ to achieve ϕ_{di} for i=1, ···, m.
4. Synthesize an appropriate compensator, C(s), to satisfy 3.
5. Using root locus, determine a suitable gain.

Remarks

1. If H(s) is positive real, it is easily seen that $\phi_i = 180°$.
2. If p_i has large damping, then the analysis above breaks down because (4) does not approximate (3).
3. This design procedure is primarily useful for systems with low loop gain because the departure angle approximately locates the poles in question. For large gains, the compensators obtained from this procedure may or may not be useful. This observation is illustrated in the examples.
4. The resulting phase of the compensator is usually of a notch phase design where the width of the

notch determines how many vibrational modes are affected. With a good background in Bode plot manipulation, it is possible to choose compensators of any shape where higher complexity and phase demands usually result in a higher order compensator. The examples at the end of this note illustrate this point.

5. The phase of the compensator is chosen to alter the departure angle of the vibrational mode poles. This compensation can be accomplished with a lead network to add phase, or with a lag network to subtract phase. The result of both compensators is the same, a satisfactory departure angle, but the magnitude effects are opposite and often determine the success or failure of phase compensation. Since the goal of the compensator is to add damping to the vibrational modes of the structure, these poles must be moved away from the imaginary axis without appreciably moving the other poles of the system. If the magnitude of the compensator is chosen such that the system is more sensitive to gain at the frequencies of the modes and attenuated elswhere, the gain applied through compensation will primarily affect the targeted poles. This choice enables the designer to move the structural poles without necessarily moving the other poles of the system and is often crucial to the stability and performance of the compensated system.

Examples

Example 1: COFS-I Mast

The first example is a reduced order model of the first four x-z bending modes of the COFS-I Mast[3,4]. The transfer function from the input of the tip proof mass actuator to a colocated velocity measurment is given by

$$P(s) = \frac{3.4s^3((s+.02)^2+7.7^2)((s+.1)^2+23.8^2)((s+.2)^2+42.4^2)}{((s+.02)^2+1.1^2)((s+.05)^2+8.7^2)((s+.13)^2+25^2)((s+.2)^2+43^2)}. \quad (5)$$

Using velocity feedback with gain, the root locus is plotted in Figure 3. The third and fourth mode poles depart satisfactorily at 180° and do not require compensation. The first mode pole is not stable for any range of gain and must be compensated. The departure angle ϕ_1, from the first mode pole is $-14°$. Since ϕ_{di} is 180°,

$$\phi_{di} - \phi_i = 180° - (-14°) = \arg(C(j\omega{=}1.1)) = 194° = -166°. \quad (6)$$

Equation (6) shows there is a choice of lead (adding phase) or lag (subtracting phase) compensation.

At this point, both lead and lag are considered to note the effect on the system magnitude response. The lag compensator transfer function is

$$C_{lag}(s) = \frac{s^2 + 6.6s + 21.6}{s^2 + .44s + .098} \tag{7}$$

and the corresponding lead compensator is

$$C_{lead}(s) = \frac{1}{C_{lag}(s)} \tag{8}$$

These second order compensators subtract or add 140 degrees of phase at 1.1 rad/s (the value of the imaginary part of the first mode pole) which would bring the departure angle of the first mode pole around in the vicinity of 180°. The phase plot of the lag compensator is shown in Figure 4.

Next, the magnitude effects of these two compensators are considered. Figure 5 shows the magnitude response of the compensated system for each of the compensators. It is seen that the lag network results in a system that is sensitive to gain at the mode frequencies and attenuated elswhere. The lead system does not attenuate high frequencies as well and therefore causes appreciable pole movement for higher frequencies thus limiting the gain achievable before the high modes cross the $j\omega$-axis. It is also seen that the lag network adjusts the second mode pole ($\phi_2 = -145$) such that it departs near 180° while the lead moves it in the wrong direction. This is important since we do not want to destabilize other modes or change the departure angle such that it departs closer to the $j\omega$-axis. Using the lag network, the root locus of the compensated system is seen in Figure 6. A comparison of the open loop and closed loop time response is seen in Figure 7. The system shows a marked increase in damping. Similar results were reported by Ham, Greeley, and Henniges[4].

Example 2: Flexible Slewing Beam

The system for this example is a vertical D.C. servomotor with a flexible slewing beam clamped to the armature shaft (See, for example, Robertshaw[5]). The beam has instrumented with a modal domain fiber optic sensor[6]. This sensor has an output which is proportional to the integral of strain along the beam. The system transfer function is

$$P(s) = \frac{-2.3\, s(s+1.15)((s+.5)^2+61^2)}{((s+.4)^2+4.8^2)((s+1.3)^2+3.3^2)}. \tag{9}$$

As seen in Figure 8, the open loop departure angle for the first and second modes are 85° and −92° respectively. In this example, the first mode pole needs to have phase added and the second mode pole needs phase subtracted to get the departure angles in the right direction. A compensator of the form

$$C(s) = \frac{150(2s+1)}{(.05s+1)(.1s+1)} \tag{10}$$

results in the frequency response of Figure 9 and the compensator root locus of Figure 10. This example shows that the compensator need not be of second order form discussed in Wie and Byun[1]. In fact, the compensators presented there result in a system with a low gain margin. Also, note that for large gains the system will become unstable.

Conclusions

In this note, we have presented a procedure based on classical techniques for the design of a low order compensator to add damping to the vibrational modes of a flexible structure. This procedure yields the compensators similar to thoses discussed in the paper by Wie and Byun[1], but allows more diversity in the pole zero structure.

References

[1] B. Wie, and K. Byun, "New Generalized Structural Filtering Concept for Active Vibration Control Synthesis," *Journal of Guidance, Control and Dynamics*, vol 12, 1989, pp 147-154.

[2] Dr. Joe Chow, R.P.I. , Personal Communication.

[3] D. Lindner, T. Celano, and E. Ide, "Decentralized Control of the COFS–I Mast Using Linear D.C. Motors," *Proceedings of the American Control Conference*, Pittsburgh, PA, June 1989.

[4] F. Ham, S. Greeley, and B. Henniges, "Active Vibration Suppression for the Mast Flight System," *IEEE Control Systems Magizine*, vol. 9, no. 1, Jan. 1989, pp 85–90.

[5] J. Juang, L. Horta, and H. Robertshaw, "A Slewing Control Experiment for Flexible Structures," *Journal of Guidance, Control, and Dynamics*, Vol. 9, 1986, pp 599-607.

[6] N. Shankaranarayanan, K. Srinivas, and R. Claus, "Mode–Mode Interference Effects in Axially Strained Few–Mode Optical Fibers", *Proc. of SPIE Fiber Optic and Lasers Sensors V, Vol* 838, 1987.

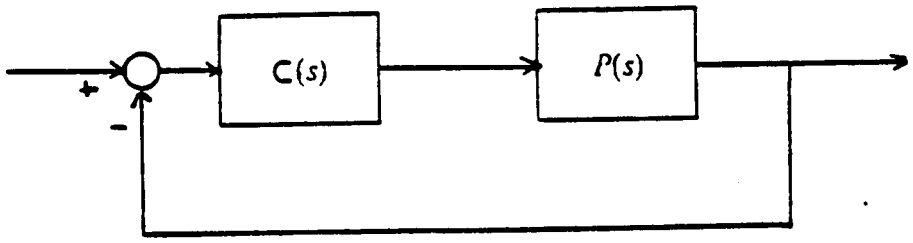

Figure 1. Negative unity feedback control system

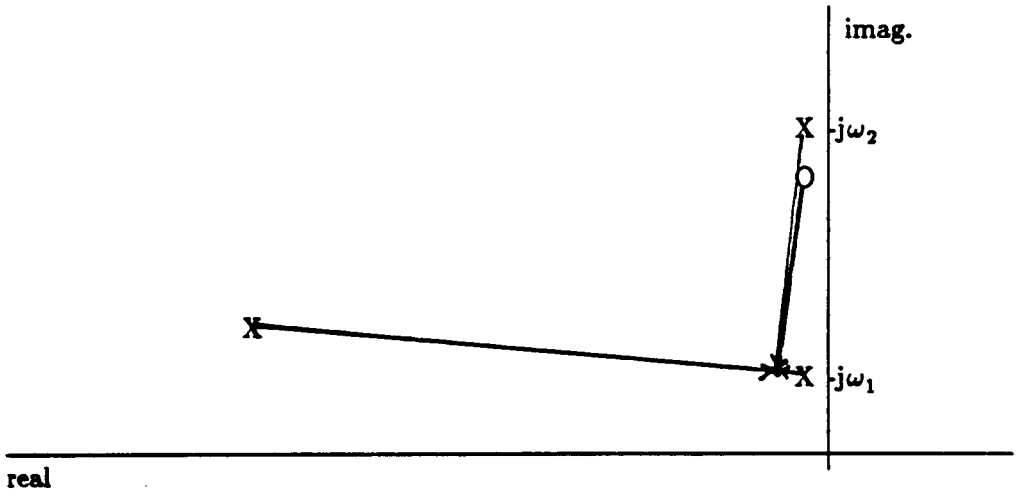

Figure 2. Determination of departure angle

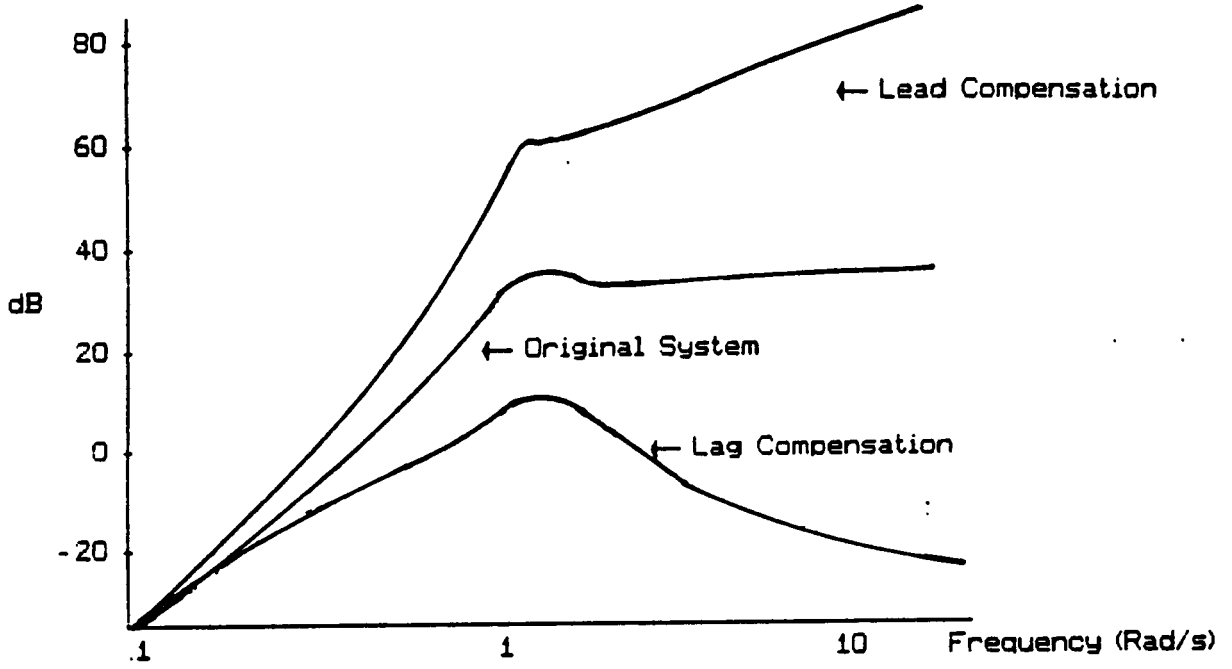

Figure 5. Frequency response of C(s)P(s)

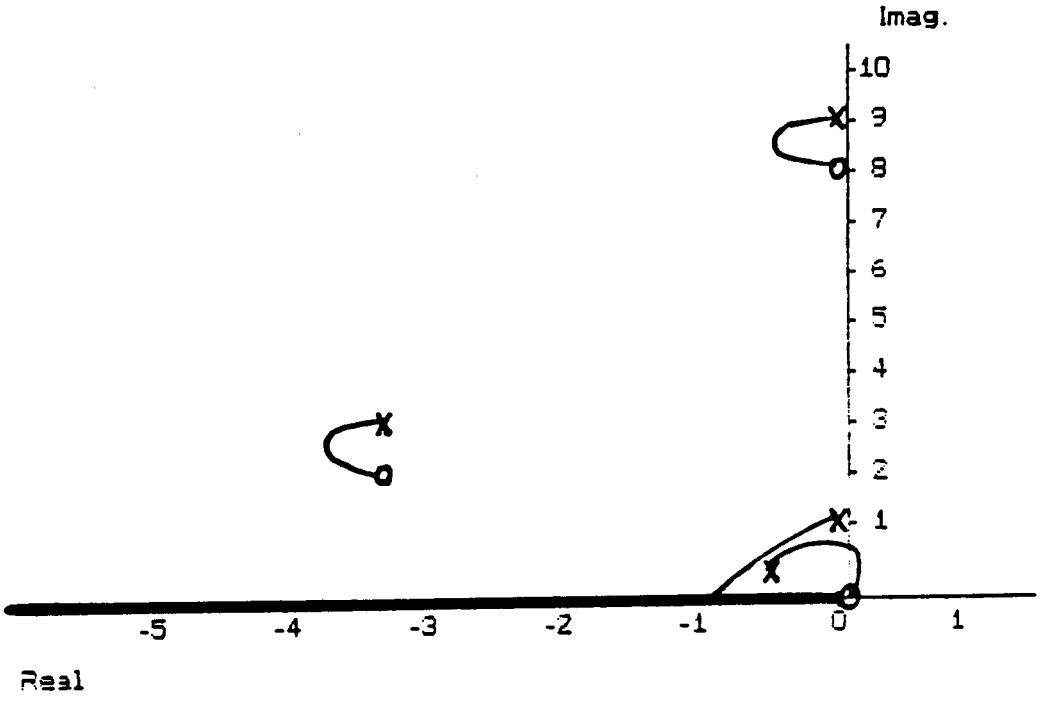

Figure 6. Root locus of $C_{lag}(s)P(s)$

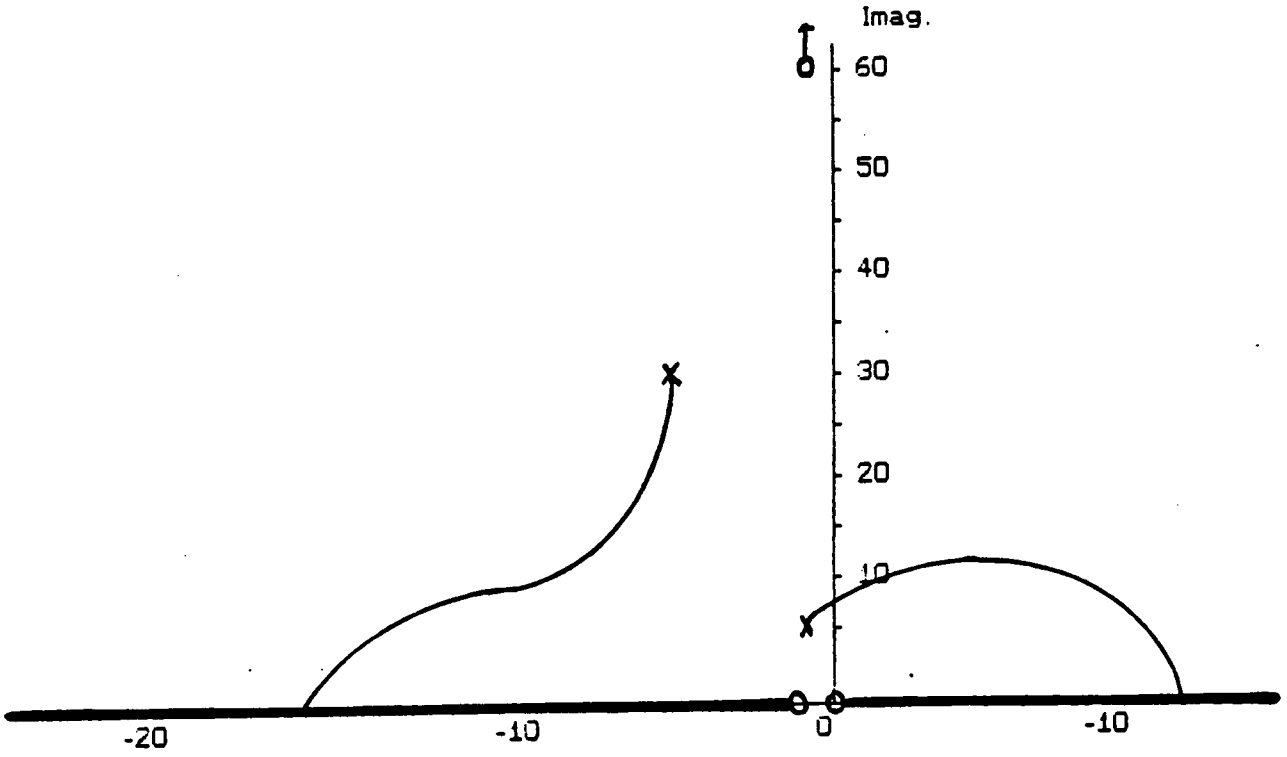

Figure 8. Root locus of slewing beam with gain feedback.

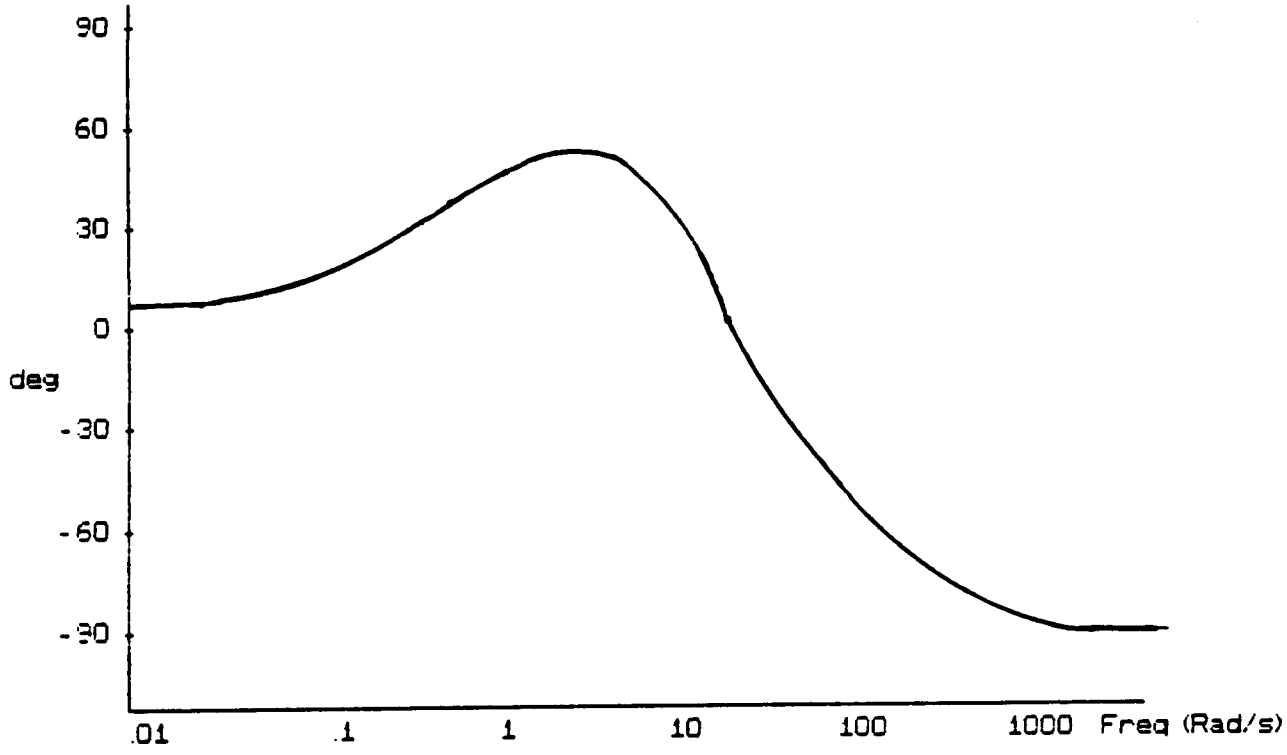

Figure 9. Phase of the compensator.

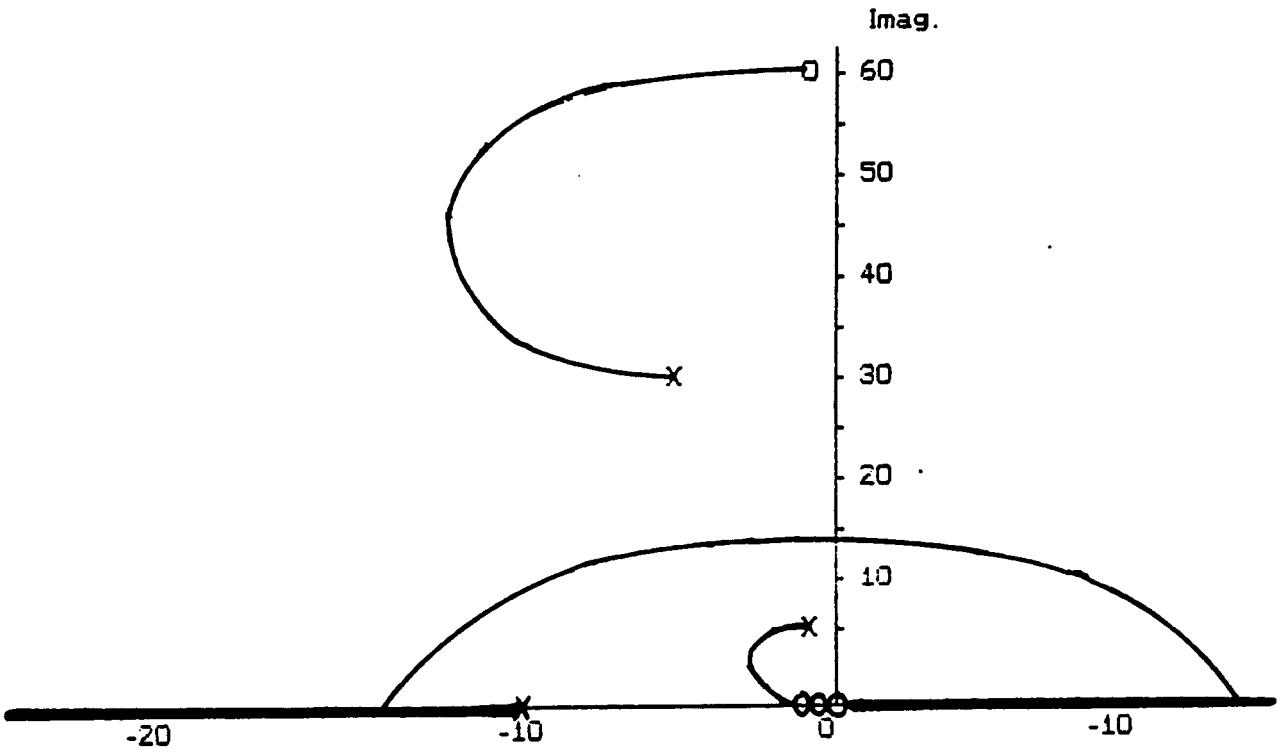

Figure 10. Root locus of the compensated slewing beam.